Nucl. Fusion **49** (2009) 104016 (14pp) doi:10.1088/0029-5515/49/10/104016

Overview of results from the National Spherical Torus Experiment (NSTX)

D.A. Gates[1], J. Ahn[2], J. Allain[3], R. Andre[1], R. Bastasz[4], M. Bell[1], R. Bell[1], E. Belova[1], J. Berkery[5], R. Betti[6], J. Bialek[5], T. Biewer[7], T. Bigelow[8], M. Bitter[1], J. Boedo[2], P. Bonoli[7], A. Boozer[5], D. Brennan[9], J. Breslau[1], D. Brower[10], C. Bush[8], J. Canik[8], G. Caravelli[11], M. Carter[8], J. Caughman[8], C. Chang[12], W. Choe[13], N. Crocker[10], D. Darrow[1], L. Delgado-Aparicio[11], S. Diem[1], D. D'Ippolito[14], C. Domier[15], W. Dorland[16], P. Efthimion[1], A. Ejiri[17], N. Ershov[18], T. Evans[19], E. Feibush[1], M. Fenstermacher[20], J. Ferron[19], M. Finkenthal[11], J. Foley[21], R. Frazin[22], E. Fredrickson[1], G. Fu[1], H. Funaba[23], S. Gerhardt[1], A. Glasser[24], N. Gorelenkov[1], L. Grisham[1], T. Hahm[1], R. Harvey[18], A. Hassanein[3], W. Heidbrink[25], K. Hill[1], J. Hillesheim[10], D. Hillis[8], Y. Hirooka[23], J. Hosea[1], B. Hu[6], D. Humphreys[19], T. Idehara[26], K. Indireshkumar[1], A. Ishida[27], F. Jaeger[8], T. Jarboe[28], S. Jardin[1], M. Jaworski[22], H. Ji[1], H. Jung[13], R. Kaita[1], J. Kallman[1], O. Katsuro-Hopkins[5], K. Kawahata[23], E. Kawamori[17], S. Kaye[1], C. Kessel[1], J. Kim[29], H. Kimura[30], E. Kolemen[1], S. Krasheninnikov[2], P. Krstic[8], S. Ku[12], S. Kubota[10], H. Kugel[1], R. La Haye[19], L. Lao[19], B. LeBlanc[1], W. Lee[29], K. Lee[15], J. Leuer[19], F. Levinton[21], Y. Liang[15], D. Liu[25], N. Luhmann Jr[15], R. Maingi[8], R. Majeski[1], J. Manickam[1], D. Mansfield[1], R. Maqueda[21], E. Mazzucato[1], D. McCune[1], B. McGeehan[31], G. McKee[32], S. Medley[1], J. Menard[1], M. Menon[33], H. Meyer[34], D. Mikkelsen[1], G. Miloshevsky[3], O. Mitarai[35], D. Mueller[1], S. Mueller[2], T. Munsat[36], J. Myra[14], Y. Nagayama[23], B. Nelson[28], X. Nguyen[10], N. Nishino[37], M. Nishiura[23], R. Nygren[4], M. Ono[1], T. Osborne[19], D. Pacella[38], H. Park[29], J. Park[1], S. Paul[1], W. Peebles[10], B. Penaflor[19], M. Peng[8], C. Phillips[1], A. Pigarov[2], M. Podesta[25], J. Preinhaelter[39], A. Ram[7], R. Raman[28], D. Rasmussen[8], A. Redd[28], H. Reimerdes[5], G. Rewoldt[1], P. Ross[1], C. Rowley[1], E. Ruskov[25], D. Russell[14], D. Ruzic[22], P. Ryan[8], S. Sabbagh[5], M. Schaffer[19], E. Schuster[40], S. Scott[1], K. Shaing[32], P. Sharpe[41], V. Shevchenko[34], K. Shinohara[30], V. Sizyuk[3], C. Skinner[1], A. Smirnov[18], D. Smith[1], S. Smith[1], P. Snyder[19], W. Solomon[1], A. Sontag[8], V. Soukhanovskii[20], T. Stoltzfus-Dueck[1], D. Stotler[1], T. Strait[19], B. Stratton[1], D. Stutman[11], R. Takahashi[9], Y. Takase[17], N. Tamura[23], X. Tang[24], G. Taylor[1], C. Taylor[3], C. Ticos[24], K. Tritz[11], D. Tsarouhas[3], A. Turrnbull[19], G. Tynan[2], M. Ulrickson[4], M. Umansky[20], J. Urban[39], E. Utergberg[19], M. Walker[19], W. Wampler[4], J. Wang[24], W. Wang[1], A. Welander[19], J. Whaley[4], R. White[1], J. Wilgen[8], R. Wilson[1], K. Wong[1], J. Wright[7], Z. Xia[15], X. Xu[20], D. Youchison[4], G. Yu[2], H. Yuh[21], L. Zakharov[1], D. Zemlyanov[3] and S. Zweben[1]

[1] Princeton Plasma Physics Laboratory, Princeton, NJ 08543, USA
[2] University of California at San Diego, San Diego, CA, USA
[3] Purdue University, Purdue, IA, USA
[4] Sandia National Laboratory, Albuquerque, NM, USA
[5] Columbia University, New York, NY, USA
[6] University of Rochester, Rochester, NY, USA
[7] Massachusetts Institute of Technology, Cambridge, MA, USA
[8] Oak Ridge National Laboratory, Oak Ridge, TN, USA
[9] University of Tulsa, Tulsa, OK, USA
[10] University of California at Los Angeles, Los Angeles, CA, USA
[11] Johns Hopkins University, Baltimore, MD, USA
[12] New York University, New York, NY, USA
[13] KAIST, Yuseong-gu, Daejon, Korea
[14] Lodestar Research Corporation, Boulder, CO, USA
[15] University of California at Davis, Davis, CA, USA
[16] University of Maryland, College Park, MD, USA

[17] University of Tokyo, Tokyo, Japan
[18] CompX, Del Mar, CA, USA
[19] General Atomics, San Diego, CA, USA
[20] Lawrence Livemore National Laboratory, Livermore, CA, USA
[21] Nova Photonics, Inc., Princeton, NJ, USA
[22] University of Illinois at Urbana–Champaign, Urbana, IL, USA
[23] NIFS, Oroshi, Toki, Gifu, Japan
[24] Los Alamos National Laboratory, Los Alamos, NM, USA
[25] University of California at Irvine, Irvine, CA, USA
[26] Fukui University, Fukui City, Fukui, Japan
[27] Niigata University, Niigata, Japan
[28] University of Washington at Seattle, Seattle, WA, USA
[29] POSTECH, Pohang, Korea
[30] JAEA, Naka, Ibaraki, Japan
[31] Dickinson College, Carlisle, PA, USA
[32] University of Wisconsin-Madison, Madison, WI, USA
[33] Think Tank Inc., Silver Springs, MD, USA
[34] UKAEA Culham Science Centre, Abingdon, Oxfordshire, UK
[35] Kyushu Tokai University, Kumamoto, Japan
[36] University of Colorado at Boulder, Boulder, CO, USA
[37] Hiroshima University, Hiroshima, Japan
[38] ENEA, Frascati, Italy
[39] Institute of Plasma Physics, AS CR, Prague, Czech Republic
[40] Lehigh University, Bethlehem, PA, USA
[41] Idaho National Laboratory, Idaho Falls, ID, USA

Received 11 December 2008, accepted for publication 9 Mar 2009
Published 10 September 2009
Online at stacks.iop.org/NF/45

Abstract
The mission of the National Spherical Torus Experiment (NSTX) is the demonstration of the physics basis required to extrapolate to the next steps for the spherical torus (ST), such as a plasma facing component test facility (NHTX) or an ST based component test facility (ST-CTF), and to support ITER. Key issues for the ST are transport, and steady state high β operation. To better understand electron transport, a new high-k scattering diagnostic was used extensively to investigate electron gyro-scale fluctuations with varying electron temperature gradient scale length. Results from $n = 3$ braking studies are consistent with the flow shear dependence of ion transport. New results from electron Bernstein wave emission measurements from plasmas with lithium wall coating applied indicate transmission efficiencies near 70% in H-mode as a result of reduced collisionality. Improved coupling of high harmonic fast-waves has been achieved by reducing the edge density relative to the critical density for surface wave coupling. In order to achieve high bootstrap current fraction, future ST designs envision running at very high elongation. Plasmas have been maintained on NSTX at very low internal inductance $l_i \sim 0.4$ with strong shaping ($\kappa \sim 2.7$, $\delta \sim 0.8$) with β_N approaching the with-wall β-limit for several energy confinement times. By operating at lower collisionality in this regime, NSTX has achieved record non-inductive current drive fraction $f_{NI} \sim 71\%$. Instabilities driven by super-Alfvénic ions will be an important issue for all burning plasmas, including ITER. Fast ions from NBI on NSTX are super-Alfvénic. Linear toroidal Alfvén eigenmode thresholds and appreciable fast ion loss during multi-mode bursts are measured and these results are compared with theory. The impact of $n > 1$ error fields on stability is an important result for ITER. Resistive wall mode/resonant field amplification feedback combined with $n = 3$ error field control was used on NSTX to maintain plasma rotation with β above the no-wall limit. Other highlights are results of lithium coating experiments, momentum confinement studies, scrape-off layer width scaling, demonstration of divertor heat load mitigation in strongly shaped plasmas and coupling of coaxial helicity injection plasmas to ohmic heating ramp-up. These results advance the ST towards next step fusion energy devices such as NHTX and ST-CTF.

PACS numbers: 52.55.Fa, 52.50.Gj, 52.25.Fi, 52.35.Ra, 52.50.Qt

1. Introduction

The spherical torus (ST) concept [1] has been proposed as a potential fusion reactor [2] as well as a component test facility (ST-CTF) [3]. The National Spherical Torus Experiment (NSTX) [4], which has been in operation since 1999, has as its primary mission element to understand and utilize the advantages of the ST configuration by establishing attractive ST operating scenarios and configurations—in particular, high-β, steady state scenarios with good confinement. As an additional mission element, NSTX exploits its unique capabilities to complement the established tokamak database

and thereby supports ITER by expanding the breadth of the range of operating parameters such as lower A, very high β, high $v_{\text{fast}}/v_{\text{Alfvén}}$, as well as other important plasma parameters. This broader range of experience helps clarify uncertainties in extrapolating to ITER by removing existing degeneracies in physics scalings. The third main element of the NSTX mission is to understand the physics properties of the ST, brought about by operating in this unique regime. Understanding the physics of the ST provides the basic framework for success with the first two mission elements described above.

With the mission elements described above as a guide for determining research priorities, the NSTX program is organized according to basic science topics which will be covered in the following sections: section 2—transport and turbulence physics, section 3—boundary physics, section 4—MHD physics, section 5—waves physics, section 6—fast particle physics, section 7—solenoid-free startup, and section 8—advanced scenarios and control. This paper will describe progress in each of these areas over the 2007–2008 period, following these topical divisions. Also, this period saw the execution of experiments done in response to explicit ITER requests for data which are direct inputs to the design review process. These topics are covered in the final section, section 9—research in direct support of ITER, just before the summary.

2. Transport and turbulence physics

2.1. Electron energy transport

The cause of anomalous electron energy transport in toroidal confinement devices is still an outstanding issue. There are numerous examples of potential explanations of this important phenomenon in the literature (see, e.g. [5–7]) invoking differing turbulent processes. However, due to the fundamental difficulty of measuring turbulence on the electron length scale, the experimental data to test these theories have been absent. Because of its relatively low magnetic field and high plasma temperature, both of which tend to increase the scale length of the electron gyro-scale turbulence, the ST is in many ways an ideal configuration on which to carry out research on the important topic of electron turbulent energy transport.

To facilitate this research, a microwave scattering diagnostic has been developed and deployed on NSTX. The system is capable of a spatial resolution of ± 2.5 cm together with a wave number resolution of $\pm 1\,\text{cm}^{-1}$, measuring predominantly k_r in the range from 2 to $24\,\text{cm}^{-1}$ [8]. By using steerable optics nearly the entire plasma minor radius can be sampled. Dedicated scans which measured the fluctuation amplitude as a function of both k_r and minor radius were performed in a variety of plasma conditions.

An illustrative example, which was originally published in [9] and appears in more detail in [10], is shown in the top frame of figure 1. Shown are the electron temperature profiles and the frequency spectra of the fluctuations with $k_r \sim 11\,\text{cm}^{-1}$, corresponding to $k_\perp \rho_e \sim 0.25$ at two times in a discharge during and after the application of 1.6 MW of electron heating power from the NSTX high harmonic fast wave (HHFW) system. The high-k scattering volume was set

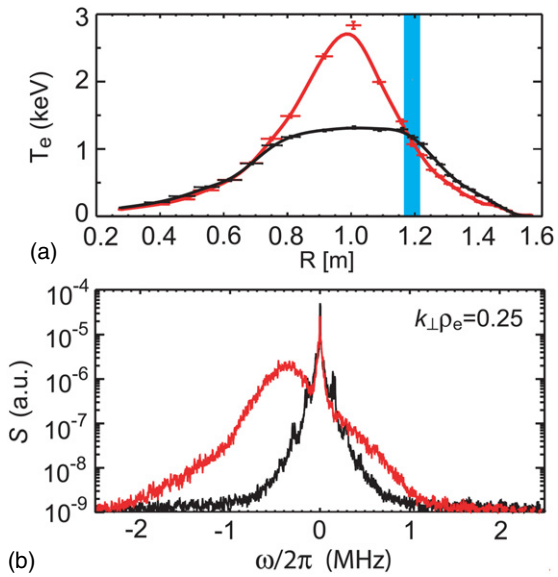

Figure 1. (*a*) The electron temperature profiles for two shots with strongly varying L_{T_e} and (*b*) the spectral power density of fluctuations with $k_\perp = 11\,\text{cm}^{-1}$.

at the inflection point of the electron temperature profile as indicated by the blue band in the figure. For this particular discharge, the variation of the electron temperature gradient (ETG) scale length $L_{T_e} \equiv T_e(\text{d}T_e/\text{d}r)^{-1}$ was from 15 cm (red) to 50 cm (black). The measured spectral density for $k_\perp = 11\,\text{cm}^{-1}$, shown in the second panel of figure 1, shows a much higher fluctuation amplitude for large values of the normalized inverse temperature gradient scale length R/L_{T_e}. Negative frequencies in the figure correspond to fluctuations propagating in the electron direction.

To gain insight into the origin of the observed fluctuation spectrum, a linear version of the GS2 stability code [11] was used to obtain the normalized critical gradient $(R/L_{T_e})_{\text{crit}}$ for the onset of the ETG instability. This code solves the gyro-kinetic Vlasov–Maxwell equations, including both passing and trapped particles, electromagnetic effects and a Lorentz collision operator. The results are shown in figure 2, where the critical gradient is compared with the measured normalized temperature gradient R/L_{T_e} for the case of figure 1. Also shown in the figure is the critical gradient scale length according to the relation described in [12]. From this, we conclude that the ETG mode is indeed unstable over most of the RF pulse where the ETG is greater than the critical gradient.

2.2. Ion energy transport

Because of its low magnetic field and strong uni-directional neutral beam heating, NSTX operates with very high levels of $E \times B$ flow shear with $\gamma_{E\times B} \sim 1$ MHz, which is up to five times larger than the typical value of the maximum growth rate of ion temperature gradient (ITG) modes [13] as calculated by the GS2 code. This means that for these cases we expect turbulence on the ion scale length to be suppressed and that transport physics will be determined by other phenomena.

To test the hypothesis that ion turbulent transport is suppressed an experiment was performed using the $n = 3$

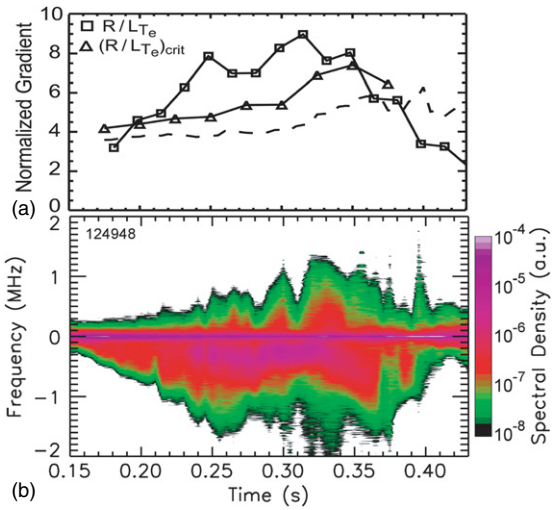

Figure 2. (*a*) The time evolution of measured gradient R/L_{T_e} (squares) and GS2 critical gradient $(R/L_{T_e})_{crit}$ for the onset of the ETG mode (triangles). The dashed line is the critical gradient from [12] and (*b*) the time history of the spectral power density of fluctuations with $k_\perp \rho_e = 0.2$–0.4 at $R = 1.2$ m. Negative frequencies correspond to wave propagation in the electron diamagnetic direction.

non-resonant braking capability [14] available on NSTX. A predominantly $n = 3$ error field (EF) is applied to the plasma using the NSTX non-axisymmetric coils, which has the effect of reducing the edge plasma rotation and creating a region of low velocity shear. The ion thermal diffusivity was determined using the TRANSP code [15] based on magnetic plasma reconstructions and the data from the entire NSTX profile dataset (T_e, n_e from Thomson scattering at 30 radial points and 16 ms temporal resolution, T_i, n_i from charge exchange recombination spectroscopy at 51 radial points with 10 ms temporal resolution and B_θ/B_ϕ from motional Stark-effect polarimetry with 16 radial points and 10 ms temporal resolution).

Shown in figure 3 are the results from the above analysis for a series of discharges for which the $n = 3$ braking current was varied from 0 A (green) to 500 A (blue), to 800 A (red). Also shown in the figure is the measured velocity shear profile for each of the discharges. It can be seen that in the outer region of the profile the ion diffusivity increases as the velocity shear decreases, with good spatial correlation between the measured change in velocity and the reduced confinement. These observations are consistent with the conclusion that the turbulence-driven ion energy loss goes from sub-dominant ($\chi_i \sim \chi_{i_{neo}}$) to dominant (4× neoclassical diffusivity) as the velocity shear is reduced.

2.3. Momentum transport

Because of the importance of $E \times B$ shear in stabilizing instabilities over the $k_\perp \rho_i \sim 1$ range of wavelengths, it is important to understand the mechanisms that determine the transport of momentum in toroidal devices. In the regime of reduced ion-scale turbulence, it is still possible to infer the effect of the residual turbulence on transport by studying the transport of momentum. This is because, whereas the neoclassical ion thermal diffusivity is large compared with the calculated turbulent ion thermal diffusivity, the neoclassical momentum transport is negligible in comparison with the residual turbulent transport of momentum. Shown in figure 4 are the measured and calculated neoclassical momentum and thermal diffusivities as determined by the TRANSP and GTC-Neo codes, respectively [16]. This result indicates that the primary driver for the momentum transport on NSTX is something other than neoclassical transport. Momentum pinch velocities have also been shown to be consistent with residual low-k turbulence drive [17, 18].

3. Boundary physics

3.1. Lithium wall coating

In 2007, the lithium evaporator (LITER) previously employed on NSTX [19] was upgraded to allow a higher operating temperature and thereby allow higher evaporation rates. The reservoir and the exit duct were also enlarged and re-aimed to optimize the deposition geometry. Lithium deposition rates up to about 60 mg min^{-1} were used and the amount of lithium applied prior to a discharge ranged from a few milligrams to over 2 g, with a total of 93 g of lithium being evaporated during the year. The improved lithium deposition rate allowed for the routine application of lithium between discharges, permitting for the first time the accumulation of a statistical database showing the effect of lithium coatings on confinement. The average relative increase in the electron stored energy due to lithium was observed to be ∼44%.

In 2008, the lithium evaporator system was further expanded [20] to include a second LITER to provide more complete coverage of the divertor since the pumping effect of lithium is proportional to the surface coverage. The improved lithium coverage led to a further increase in the observed confinement improvement. For reference discharges, the average relative increase in electron stored energy with the dual LITER was 44%, nearly double that achieved with a single LITER. As was the case in 2007, the bulk of the increase in total plasma stored energy was in the electron channel. The electron stored energy plotted versus the total stored energy is shown in figure 5. The addition of the second evaporator also enabled the development of an operational scenario that did not rely on helium discharge cleaning. The no-glow scenario decreased the time between plasma discharges and reduced helium contamination in subsequent discharges.

Another important effect of the application of lithium coatings was the reliable transition to edge localized mode (ELM)-free H-mode. This effect is illustrated in figure 6. The figure begins with a plasma discharge which preceded the application of lithium, followed by data from a series of discharges with increasing levels of lithium deposition. The steady increase in the duration of the ELM-free periods as the lithium coating is increased is apparent. With thicker coatings yet, ELMs are suppressed entirely. It should be pointed out that the discharge subsequently suffers from the often observed impurity accumulation associated with ELM-free operation.

3.2. Scrape-off layer (SOL) width scaling

Owing to geometric factors and generally high power density as characterized by the parameter P/R, the outer divertor peak

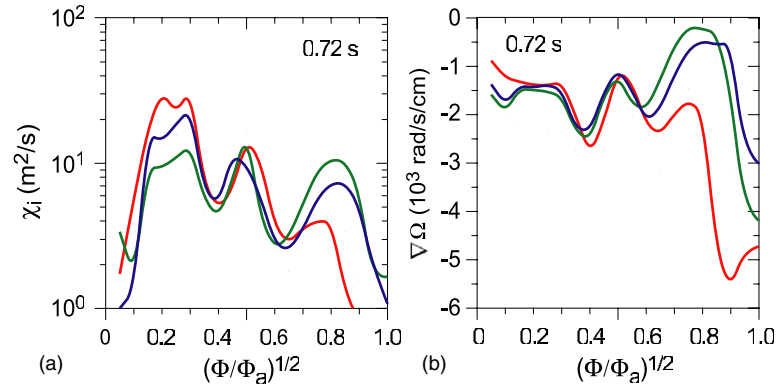

Figure 3. (*a*) The measured ion thermal diffusivity and (*b*) the measured velocity shear varying the applied $n = 3$ braking torque with braking coil currents of (1) 0 A (green), (2) 500 A (blue) and (3) 800 A (red).

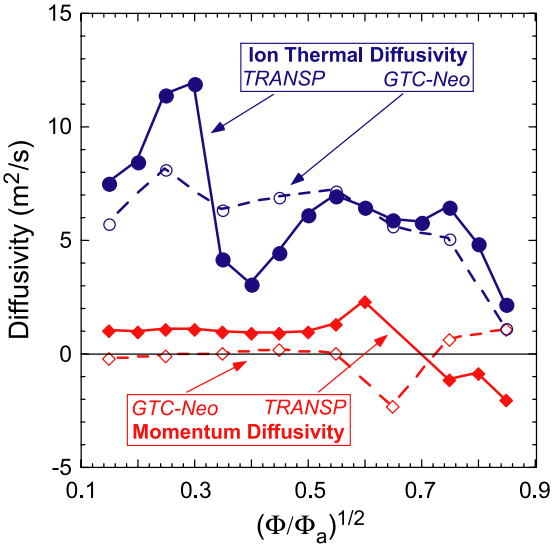

Figure 4. The measured ion thermal and momentum diffusivity compared with that predicted by GTC-Neo [16].

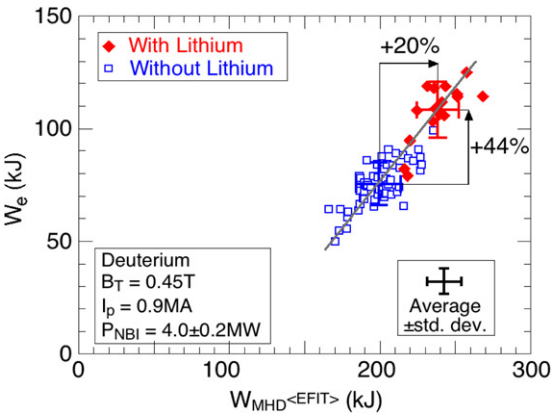

Figure 5. The increase in electron thermal stored energy plotted versus total plasma stored energy for data from standard reference discharges in 2008.

heat flux in excess of 10 MW m^{-2} has been measured in NSTX [21]. While this high heat flux has been handled both through active puffing for divertor detachment [22] and shaping to increase the divertor footprint [23, 24], future machine design

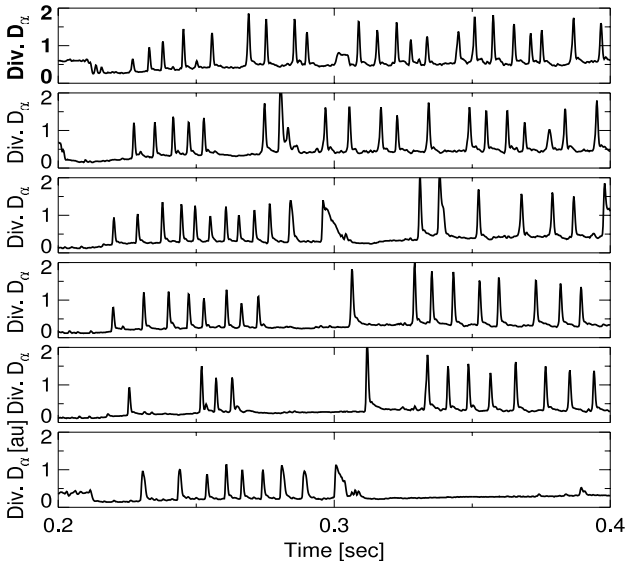

Figure 6. The suppression of ELMs after a sequence of shots with steady application of lithium, with the amount of applied lithium increasing from the top frame to the bottom frame.

requires an estimate of the unmitigated heat flux to assess the operating space limitations. To reliably project forward to next step devices, an understanding of the processes that set the target plate heat flux footprint is needed.

We have examined the ratio of SOL widths (projected to the outer midplane) and found the ratio of λ_{T_e}/λ_q to be consistent with parallel electron conduction being the dominant SOL heat transport mechanism on the open field lines in the near SOL [25]. Here we define the temperature SOL width λ_{T_e} to be the scale length of the temperature profile as determined from an exponential fit to the temperature profile data obtained using a reciprocating Langmuir probe near the midplane, and the power SOL width λ_q to be the scale length from an exponential function fit to data taken with an infra-red camera focussed on the divertor and then mapped to the midplane. From the parallel power balance equation, $\lambda_{T_e}/\lambda_q = 7/2$ is expected if electron conduction dominates the heat transport. In the near SOL, $\lambda_{T_e}/\lambda_q \sim 2.6$ has been measured in type V ELMy H-mode discharges (and up to 3 in ELM-free H-mode), with λ_{T_e} obtained from a fast reciprocating probe and λ_q from IR camera data mapped to the

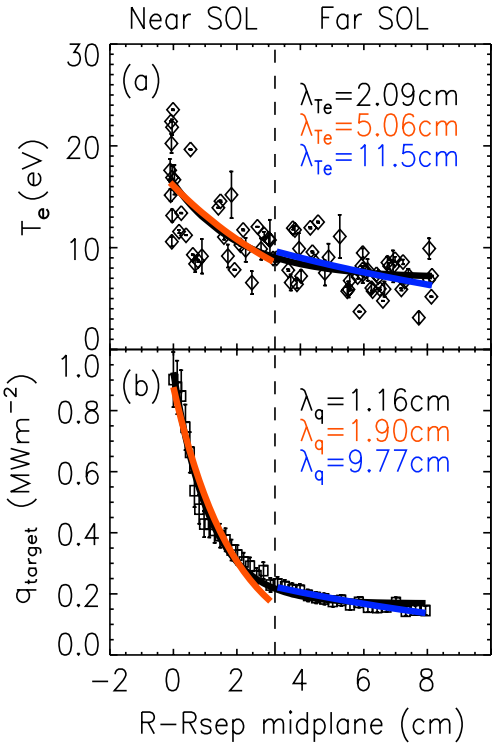

Figure 7. The measured values of λ_{T_e} and λ_q as determined from reciprocating probe data and IR camera data.

magnetic midplane, with both profiles fit to simple exponential functions (panels (*a*) and (*b*) in figure 7). It is noted that use of offset exponential fitting functions both changes the measured $\lambda_{T_e} \sim 1.8$, as well as the theoretical $\lambda_{T_e} \sim 2.2$, owing to proper substitution of the radial profile form back into the parallel power balance equation [25]. In the far SOL, very broad SOL widths are measured, characteristic of neither conduction limited nor sheath limited heat transport. In addition, the SOL widths are seen to narrow significantly with plasma current [26, 27].

3.3. Divertor heat flux reduction

Experiments conducted in high-performance H-mode discharges demonstrated that significant reduction of the divertor peak heat flux, q_{pk}, and access to detachment occurs naturally in a highly-shaped ST. Because of the high poloidal magnetic flux expansion factor, f_M, between the midplane SOL and the divertor plate strike point ($f_M \sim 18$–26) and higher SOL area expansion, the divertor particle and heat fluxes are much lower in the highly-shaped plasmas than in similar plasmas with lower shaping parameters [24]. In addition, the higher radiative plasma volume and the plasma plugging effect, counterbalancing the open configuration of the NSTX divertor, facilitate access to the radiative divertor regime with reduced heat flux.

Steady-state measurements of divertor peak heat flux in NSTX showed that q_{pk} increases monotonically with NBI heating power and plasma current [26] due to the corresponding increase in the power fraction flowing into the SOL and the decrease in the connection length (proportional to q). Access to the partially detached divertor (PDD) regime was demonstrated in 1.0–1.2 MA, 6 MW NBI-heated discharges using additional divertor deuterium injection. These discharges represent the most challenging case for divertor heat flux mitigation in NSTX as q_{pk} in the range 6–12 MW m^{-2} is routinely measured. A partial detachment of the outer strike point was induced at several gas puffing rates in 6 MW, 1.0 MA discharges while good core confinement and pedestal characteristics were maintained, as shown in figure 8. Steady-state heat flux reduction in 6 MW, 1.2 MA discharges from 4–10 to 1.5–3 MW m^{-2} required higher gas puffing rates. While core plasma confinement properties were not degraded, β-limit related disruptive magnetohydrodynamic (MHD) activity reduced the pulse length by 10–15%. The partial outer strike point detachment was evidenced by a 30–60% increase in divertor plasma radiation, a peak heat flux reduction up to 60%, measured in a 10 cm radial zone adjacent to the strike point, a 30–80% increase in divertor neutral compression and a reduction in ion flux to the plate. Divertor plasma density increased to 3–4 $\times$ 10^{20} m^{-3} and a significant volume recombination rate increase in the PDD zone was measured. At higher gas puffing rates, an X-point MARFE was formed suggesting that further radiative divertor regime optimization in NSTX would require active divertor pumping [28].

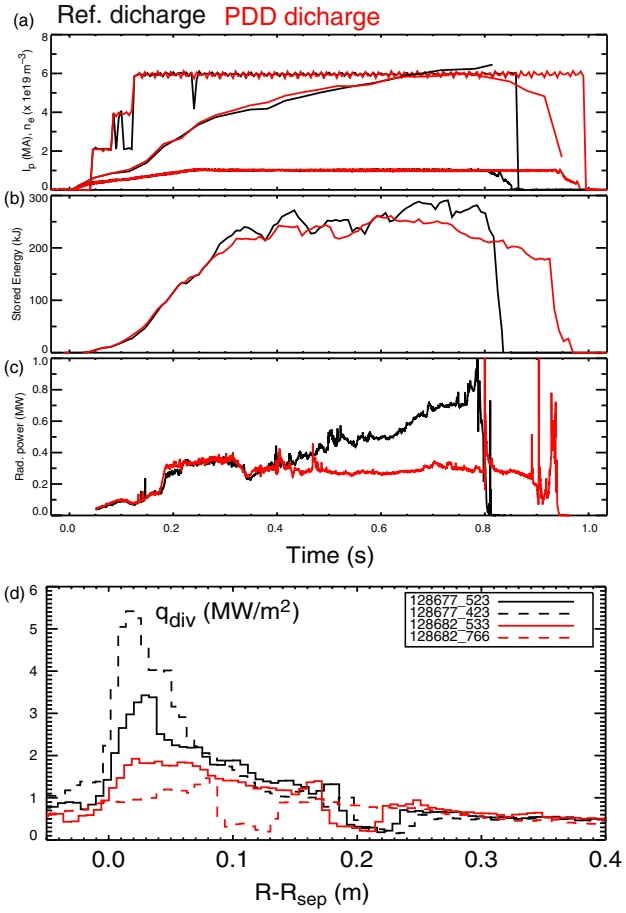

Figure 8. A reference 6 MW, 1.0 MA discharge (black) and a PDD (red) (*a*) plasma current, NBI power, and line-averaged density, (*b*) plasma stored energy, (*c*) radiated power and (*d*) divertor heat flux profiles at specified times for the two discharges.

4. MHD physics

4.1. EFs and resonant field amplification/resistive wall mode (RFA/RWM) control

At high β, correction of non-axisymmetric field errors can aid sustainment of high toroidal rotation needed for passive (rotational) stabilization of the $n = 1$ RWM and/or suppression of the $n = 1$ RFA. In 2006, algorithms were developed to correct for a toroidal field (TF) EF that results from the motion of the TF coil induced by an electromagnetic interaction between the ohmic heating (OH) and TF coils [29]. In 2007 significant emphasis was placed on utilizing improved mode detection to better identify and control the RFA/RWM and more complete understanding of the intrinsic EF. The improved RFA/RWM control used the full complement of in-vessel poloidal field sensors for mode identification, and optimized the relative phase of the upper and lower sensors to best discriminate between $n = 1$ and $n > 1$ fields. Improved detection increases the signal to noise, improves mode detection during any mode deformation, and allows for increased proportional gain during feedback-controlled RFA/RWM. In fact, in 2007, using optimized B_p sensors in the control system allowed feedback to provide all of the $n = 1$ EF correction at high beta, whereas previous $n = 1$ EF correction required an *a priori* estimate of intrinsic EF. To train the RFA/RWM control system, an $n = 1$ EF was purposely applied to reduce the plasma rotation and destabilize the $n = 1$ RWM. Then, phase scans were performed to find the corrective feedback phase that reduced the purposely applied EF currents. The gain was then increased until the applied EF currents were nearly completely nulled and plasma stability restored.

Beyond $n = 1$ EFs, $n = 3$ EFs were found to be important in NSTX, particularly at high $\beta_N \equiv \beta_t a B_t / I_p$. In experiments that varied the polarity and amplitude of an applied $n = 3$ EF, plasma pulse-lengths varied by as much as a factor of 2 depending on $n = 3$ polarity. It is noteworthy that $n > 1$ EFs are not commonly addressed in present devices, or in future devices such as ITER. Interestingly, $n = 2$ fields were also investigated but within detection limits all phases of applied $n = 2$ field were found to be deleterious to plasma performance, indicating that NSTX does not benefit from $n = 2$ error correction.

At the end of 2007, $n = 1$ RFA suppression was combined with the $n = 3$ EF correction. The scenario was so successful that it was widely utilized in 2008 to improve plasma operations. The application of both $n = 3$ correction and $n = 1$ RFA/RWM control has enabled the maintenance of plasma rotation at high-β throughout the plasma discharge. As can be seen in figure 9, the plasma rotation profile is maintained throughout the period that CHERS data are available. $\beta_N \sim 5(\%\,\mathrm{m\,T\,MA^{-1}})$ is maintained for 3–4τ_{CR}, and the plasma current flat-top is 1.6 s, an ST record at this current level. Previously long pulse discharges at high-β were limited by a slow degradation of rotation in the plasma core with the eventual onset of either a saturated internal kink mode [30] or an RWM [31].

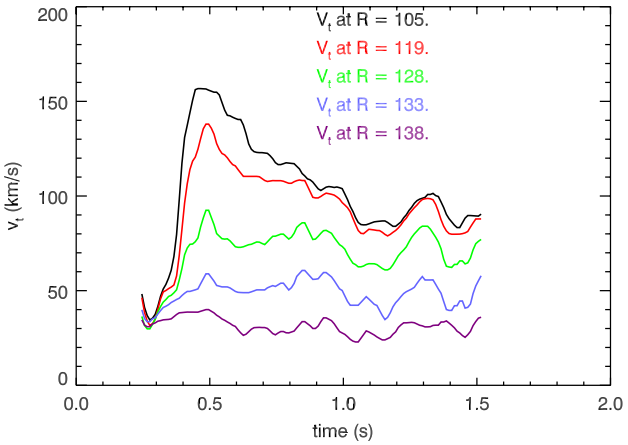

Figure 9. The measured plasma rotation at various radii plotted versus time during a discharge that utilized combined $n = 3$ EF correction and $n = 1$ RFA suppression. The plasma rotation is maintained for the duration of the discharge.

4.2. RWMs and neoclassical toroidal viscosity (NTV)

NSTX has demonstrated the stabilization of the RWM [32] by using non-resonant $n = 3$ magnetic braking [14] to slow plasma rotation below the critical rotation for stabilizing the RWM, and then stabilizing the plasma using $n = 1$ feedback. Recent experiments have probed the relationship between rotation and RWM stability. The results show greater complexity of the critical rotation, ω_{crit}, for RWM stabilization than can be explained by simple RWM models. Recent analysis looking at more complete theory of RWM stability [33] has had initial success in explaining observations. The theory includes the effects of kinetic interactions between the mode and the precession of trapped ions. Initial investigations as to whether this more complete theory can explain the physics of the observed RWM stability thresholds on NSTX have shown correct scalings of the mode onset with collisionality and rotation and have predicted the onset of instability under varying plasma conditions, as discussed in [34].

In addition, experiments investigating the physics of NTV [35] have been extended to study the effects of predominantly $n = 2$ applied fields. As expected, the $n = 2$ fields slow the plasma over a wider radial extent due to the slower fall-off the radial eigenfunction of the applied perturbation. Another advantage of the $n = 2$ braking study is that the toroidal spectrum of the applied field for this configuration has a very low $n = 1$ field component. The low $n = 1$ component eliminates any issue of resonant damping being the cause of the observed rotation reduction. Another series of experiments examined the collisionality dependence of the braking torque and found that, as T_i was raised by the application of lithium coating, the braking torque increased. The increase in torque was observed to scale as $T_{NTV} \sim T_i^{5/2}$, consistent with the predictions of theory [14, 34, 35].

4.3. The effect of rotation on neoclassical tearing modes (NTMs)

Plasma rotation and/or rotation shear are believed to play important roles in determining the stability of NTMs [36]. Results from DIII-D using mixed co/counter balance show that

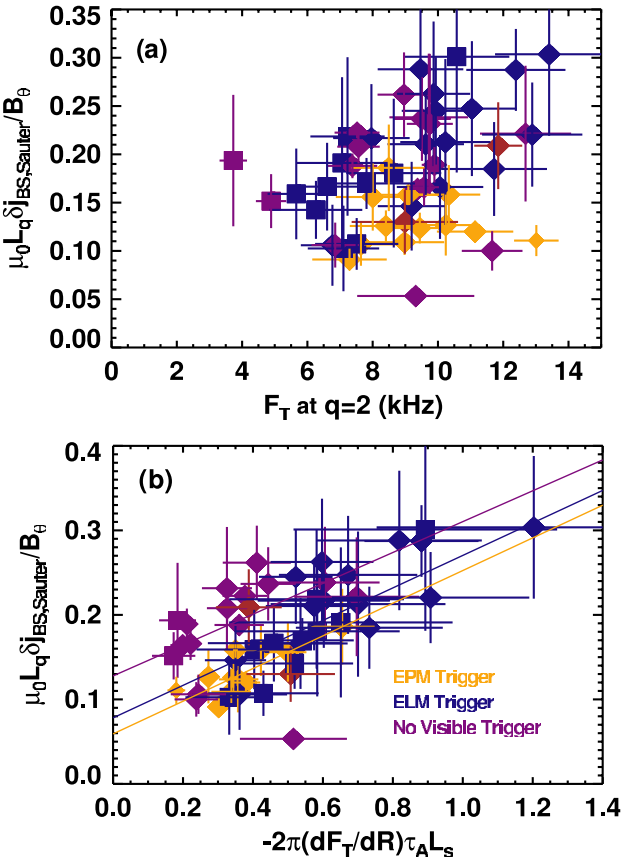

Figure 10. The variation of the magnitude of the bootstrap drive term for the NTM with (*a*) plasma rotation frequency $q = 2$ and (*b*) local rotational shear at $q = 2$.

for the 3/2 mode, the saturated $m/n = 3/2$ neoclassical islands are larger when the rotation shear is reduced. Furthermore, the onset β_N for the 2/1 mode is lower at reduced rotation and rotation shear.

Experiments in NSTX [37] have studied the onset conditions for the 2/1 mode, as a function of rotation and rotation shear, where $n = 3$ magnetic braking has been utilized to slow rotation. By studying many discharges with a range of braking levels and injection torques, a wide variety of points in rotation/rotation shear space have been achieved. Additionally, all NTM relevant quantities, such as the rotation shear and bootstrap drive for the mode, have been evaluated using correct low aspect ratio formulations.

The results of this investigation are shown in figure 10, where the bootstrap drive at NTM onset is plotted against (*a*) plasma rotation frequency at $q = 2$, and (*b*) local rotation shear at $q = 2$; larger values of drive at mode onset imply increased stability. The colour scheme is related to the triggering mechanism: the modes are observed to be triggered by energetic particle modes (EPMs, orange points), ELMs (blue points), or in some cases grow without a trigger (purple points). Considering frame (*a*), there is no clear trend in the onset threshold with rotation, either within each trigger type or considering all of the points as a group. This is in contrast to the data in (*b*), where the onset NTM drive is plotted against the rotation shear at $q = 2$. The entire set of points shows increasing drive required at larger local flow shear. Furthermore, the coloured lines show that within each trigger type, the onset threshold depends on the local rotation shear, with EPMs triggering the modes at the lowest drive, ELMs at intermediate levels and the trigger-less NTM occurring at the largest bootstrap drive. These and other NSTX results, coupled to DIII-D measurements, indicate that sheared rotation and its synergistic coupling to magnetic shear can strongly affect tearing mode stability.

5. Wave physics

5.1. HHFW heating

The NSTX HHFW system is capable of delivering 6 MW of 30 MHz heating power through a 12 strap antenna which can excite waves with $3.5\,\mathrm{m}^{-1} < |k_\parallel| < 14\,\mathrm{m}^{-1}$. Substantial progress was made on understanding coupling of HHFW to achieve efficient electron heating. The improved coupling efficiency is associated with controlling the edge plasma density to below the critical density for coupling to surface waves (where $n_{e_{crit}} \sim B \times k_\parallel^2/\omega$) [39]. Coupling control has been accomplished by both (a) reducing the edge plasma density and (b) increasing the critical density for surface wave coupling by operating at higher TF. Scaling of the heating efficiency shows good agreement with $n_{antenna} < n_{crit}$ as the relevant criterion. This is an important issue for ITER, because the ITER ICRH antenna is designed to run with relatively low $k_\parallel$, implying a low $n_{crit} \sim 1.4 \times 10^{18}\,\mathrm{m}^{-3}$.

After extensive wall conditioning which included lithium evaporation, HHFW heating in deuterium plasmas, for which control of the density had been more difficult than for helium plasmas, was as successful as that for helium plasmas [38].

Central electron temperatures of 5 keV have been achieved in both He and D plasmas with the application of 3.1 MW HHFW at $k_\parallel = -14\,\mathrm{m}^{-1}$, and at a toroidal magnetic field of $B_t = 0.55$ T, as shown in figures 11(*a*) and (*b*). These high heating efficiency results were obtained by keeping the edge density of the plasma below the critical density for perpendicular wave propagation for the chosen antenna toroidal wavenumber, presumably thereby reducing the wave fields at the edge of the plasma and the edge RF power losses [39]. The edge losses at the lower antenna phasings (longer toroidal wavelengths) are the hardest to control but a phase scan in deuterium has shown efficient heating down to the antenna phase of $k_\parallel = -7\,\mathrm{m}^{-1}$ [38, 40] and significant heating has been obtained in deuterium at $k_\parallel = -3.5\,\mathrm{m}^{-1}$ for the first time [40].

Advanced RF modelling of the HHFW wave propagation in NSTX shows that the waves propagate at a significant angle to the normal to the TF in entering the plasma, which also can enhance the interaction of the fields with the antenna and wall structures. These modelling results also predict very high single pass damping in the NSTX plasma [40], so that if the initial interaction with the antenna and wall can be suppressed by placing the onset density for perpendicular propagation away from these structures, very low edge loss will occur resulting in high heating efficiency. This makes the NSTX plasma an ideal test-bed for benchmarking models in advanced codes for RF power loss in the vicinity of the antenna as these codes are developed. Experiments have begun on

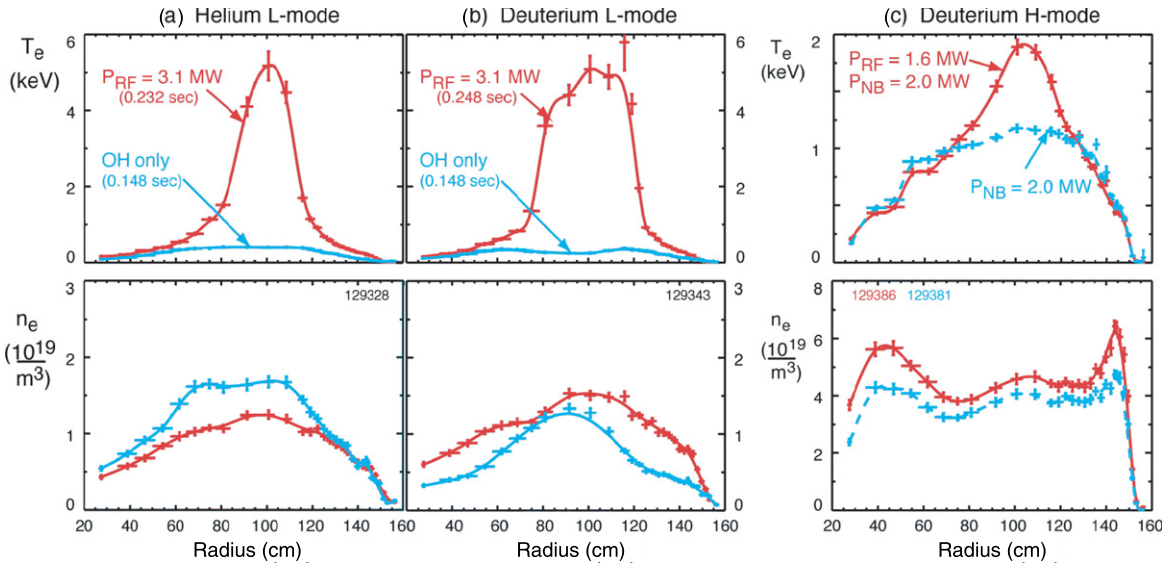

Figure 11. HHFW heating of electrons for (*a*) helium L-mode, (*b*) deuterium L-mode and (*c*) neutral beam driven H-mode deuterium discharges in NSTX (180° antenna phasing $k_\phi = 14$–$18\,\mathrm{m}^{-1}$, $B_t = 0.55\,\mathrm{T}$, and $I_p = 0.65\,\mathrm{MA}$ for (*a*) and (*b*) and $I_p = 1\,\mathrm{MA}$ for (*c*)).

NSTX to optimize HHFW core heating of neutral beam driven H-mode deuterium plasmas. Again with a well-conditioned wall, significant core electron heating, as evidenced by an increase ~0.7 keV in $T_e(0)$ and a factor of ~2 in central electron pressure shown in figure 11(*c*), has been observed for 1 MA, 0.55 T operation for an antenna phase of 180° ($k_\parallel$ = '±14 and 18 m^{-1}). This result contrasts strongly with the total lack of heating found earlier at $B_t = 0.45\,\mathrm{T}$ [41], and is useful for the study of electron transport in the NSTX core plasma.

5.2. Electron Bernstein wave (EBW) coupling studies

Significant increases in thermal EBW emission were observed with an EBW radiometer diagnostic [42] during NSTX H-mode discharges conditioned with evaporated lithium [43]. With the injection of lithium, the conversion efficiency of fundamental frequency EBW blackbody radiation at 18 GHz, emitted from near the core of NSTX H-mode plasmas and mode-converted to electromagnetic waves in the plasma edge, increased from 10% to 55–70%. Correspondingly, the second harmonic EBW transmission from near the plasma core increased from 20% to 50% with the addition of lithium plasma conditioning. Figure 12(*a*) shows the central electron temperature $T_e(0)$ time evolution for two $I_p = 0.8\,\mathrm{MA}$, H-mode plasmas, one without lithium evaporation (shot 124284, solid black line) and the other with $19\,\mathrm{mg\,min}^{-1}$ of lithium evaporation, after 286 mg of lithium had already been evaporated into the NSTX vacuum vessel (shot 124309, dashed red line). Both shots had L- to H-mode transitions at 0.14 s (indicated by the vertical dashed line in figure 12). The discharge without lithium conditioning exhibits a collapse of EBW T_{rad} from 300 eV immediately before the L- to H-mode transition to about 50–100 eV during the H-mode phase. In contrast, the plasma with lithium conditioning has a large rise in EBW T_{rad} after the L- to H-mode transition, initially to 400 eV and then to 500–600 eV later in the H-mode phase. Figure 12(*c*) shows the EBW transmission efficiency from the plasma core to the EBW radiometer antenna following mode conversion in the plasma SOL. The EBW transmission efficiency is less than 10% during the H-mode phase for the plasma without lithium conditioning but is 50–70% throughout the H-mode phase of the plasma with lithium conditioning. These EBW emission measurements have been compared with results from an EBW emission simulation code [44] that includes the magnetic plasma equilibrium and T_e and n_e profiles from laser Thomson scattering. The dramatic increase in EBW transmission efficiency with the addition of lithium evaporation during NSTX H-mode plasmas is consistent with a large decrease in EBW collisional damping prior to mode conversion in the SOL.

6. Fast particle physics

While a single toroidal Alfvén eigenmode (TAE) is not expected to cause substantial fast ion transport in ITER, multiple modes, particularly if they strongly interact, becoming non-linear as in an 'avalanche event' [45], can affect ignition thresholds, redistribute beam driven currents and damage plasma facing components (PFCs) on ITER. NSTX is an excellent device for studying these modes because of its high $v_{fast}/v_{Alfvén}$. The TAE avalanche threshold has been measured on NSTX and the concomitant fast ion losses are studied with measurements of internal mode structure, amplitude and frequency evolution and measurements of the fast ion distribution [46, 47]. Fast ion transport is studied with multi-channel neutral particle analyzer (NPA) diagnostics and fast neutron rate monitors. Of particular interest is that the NPA shows that redistribution extends down to energies at least as low as 30 keV, less than half the full energy of injection. Loss of fast ions is indicated by drops of ~10% in the neutron rate at each avalanche event as shown in figure 13. There are no other MHD events coincident with the neutron drops. The plasma equilibrium is reconstructed during the avalanching period using the equilibrium code, LRDFIT, which uses motional Stark effect (MSE) data to constrain the current profile. The NOVA code was used to find

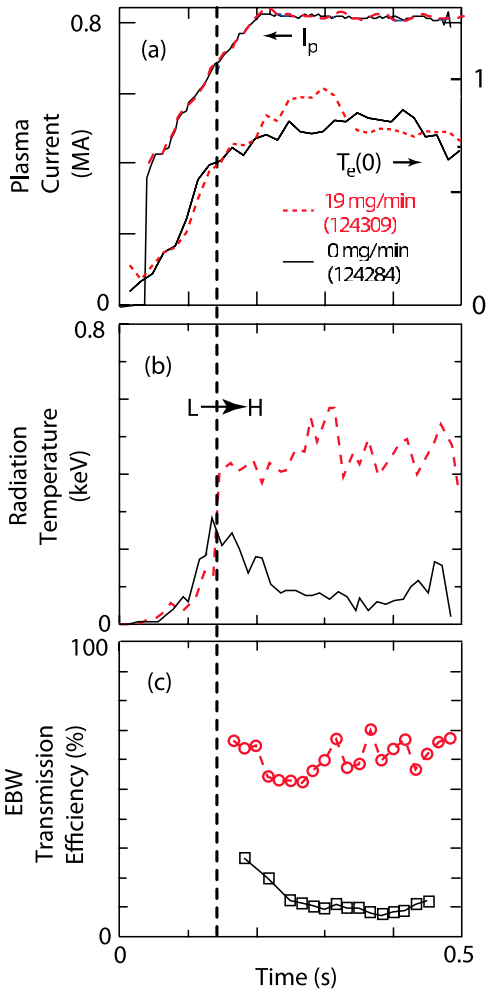

Figure 12. (*a*) Plasma current and central electron temperature evolution for two H-mode plasmas, one without lithium conditioning (black solid line) and one with lithium conditioning (red dashed line). (*b*) Time evolution of EBW radiation temperature for fundamental emission from the plasma core at 18 GHz for the two plasmas in figure 1(*a*). (*c*) EBW transmission efficiency from the core to the EBW radiometer antenna.

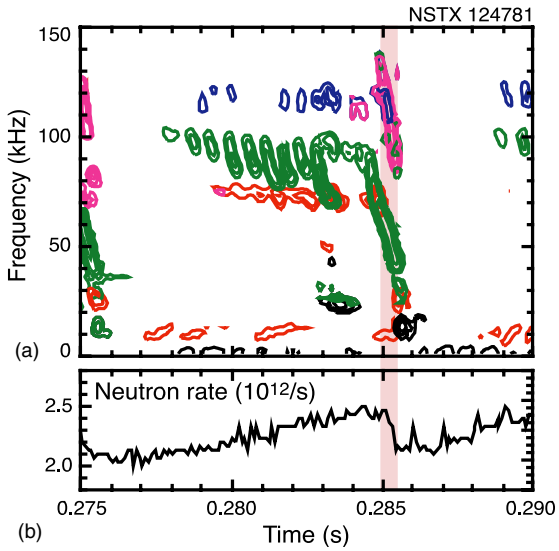

Figure 13. (*a*) Detailed spectrogram of single avalanche cycle. Colours indicate toroidal mode numbers (black 1, red 2, green 3, blue 4, magenta 6) and (*b*) neutron rate showing drop at avalanche.

eigenmode solutions for the four dominant TAE modes seen in the avalanche at 0.285 s shown in figure 13. The NOVA eigenmode structures, scaled in amplitude and frequency evolution to experimental measurements, are used to model fast ion transport with ORBIT [48, 49]. Good agreement is found for the fast ion losses at avalanche events.

7. Solenoid-free startup

Elimination of the central solenoid would be helpful for the ST concept. Solenoid-free plasma startup is also relevant to steady-state tokamak operation, as this large component that is located in a high radiation environment is needed only during the initial discharge initiation and current ramp-up phases.

Coaxial helicity injection (CHI) is a candidate both for plasma startup in the ST and for edge current drive during the sustained phase [50]. The method, which is referred to as transient CHI first demonstrated on the HIT-II experiment [51], has now been successfully used in NSTX for plasma startup and coupling to induction [52]. CHI is implemented by driving current along externally produced field lines that connect the lower divertor plates in the presence of toroidal and poloidal magnetic fields. NSTX uses the lower divertor plates as the injector. The initial injector poloidal field is produced using the lower divertor coils. This field connects the lower inner and outer divertor plates. Gas is injected in a region below the divertor plates and a capacitor bank is discharged across the lower divertor plates. Currents then flow along the poloidal field lines connecting the lower divertor plates. As the injected current exceeds a threshold value, the $J \times B$ force exceeds the restraining force from the injector field lines, causing the injected field to pull into the vessel as shown in [52]. Reconnection then occurs near the injector, producing a closed flux equilibrium in the vessel.

NSTX has demonstrated coupling of the CHI produced current to conventional inductive operation. In figure 14, we show traces for the injector current, the plasma current and the applied inductive loop voltage for a CHI-started discharge that was coupled to induction. In this discharge 1.5 kA of injector current produces about 100 kA of toroidal current. The current multiplication, defined as the ratio of the toroidal current to the injector current, peaks near 70. The highest amount of closed flux current produced in NSTX CHI discharges is 160 kA, which is a world record for non-inductive closed flux current generated during formation in a ST or tokamak. During the decay phase of this current induction is applied from the central solenoid. The plasma current then ramps up reaching a peak value of 700 kA, and the plasma to heats up to over 600 eV. Similar discharges in NSTX have transitioned into H-modes as described in [52].

8. Advanced scenarios and control

The achievement of high plasma elongation is critical to the success of the spherical torus concept, since the bootstrap fraction increases as the square of the plasma elongation for fixed normalized $\beta_N \equiv \beta_t a B_t / I_p$, where I_p is the plasma

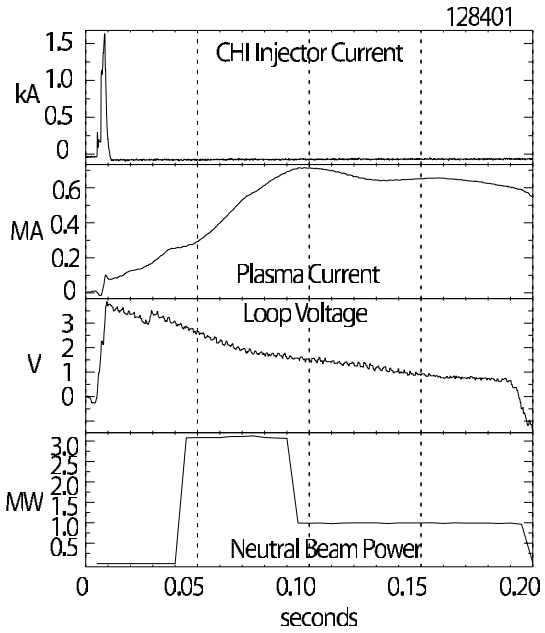

Figure 14. Shown is a discharge (128401) in which a CHI-started discharge is coupled to induction. Note that approximately 2 kA of CHI injector current produces about 100 kA of CHI produced plasma current. Application of an inductive loop voltage causes the current to ramp up to 700 kA. Application of NBI power increases the current ramp-rate.

current, B_t is the vacuum toroidal magnetic field at the plasma geometric centre, a is the plasma minor radius and β_t is the toroidal β defined as the $\beta_t = \langle P \rangle / (B_t^2/2\mu_0)$, where $\langle P \rangle$ is the pressure averaged over the plasma volume. Achieving high bootstrap current is crucial to being able to maintain a spherical torus plasma.

The primary motivation for discharge development on NSTX is the simulation of operational scenarios on proposed future ST devices such as NHTX [53] and ST-CTF [3]. It is proposed that these devices operate at very high elongation $\kappa \sim 2.7$ and with somewhat higher aspect ratio ($\sim$1.8) than typical on NSTX ($A \sim 1.3$). In 2008, discharges were developed in NSTX that investigate this regime of operation, achieving $\kappa \sim 2.7$ at $\beta_N \sim 5.5$ for 0.5 s $\sim 2\tau_{CR}$. Figure 15 shows the equilibrium cross-section for such a discharge. These discharges achieved high non-inductive current fractions $f_{NI} \sim 65\%$ and $f_{bs} \sim 50\%$, matching the previous best values on NSTX but for longer pulse. The end of these high elongation discharges is now determined by the heating limits of the TF coil on NSTX.

Another important distinction between NSTX and future STs is collisionality. NSTX, because of its modest size and low field relative to these future devices, typically runs with $0.1 \lesssim \nu_e^* \lesssim 1$ over most of the plasma cross-section, much higher than the values anticipated by devices such as NHTX and/or ST-CTF. The higher collisionality on NSTX substantially reduces the non-inductive current fraction. Using a scenario that had a lower collisionality and simultaneously achieved a record value of β_p, NSTX has been able to demonstrate that beam driven current scales according to classical predictions and that NSTX can support simultaneous higher beam driven current and high bootstrap fraction. The discharge in question used both lithium evaporation and transient techniques to

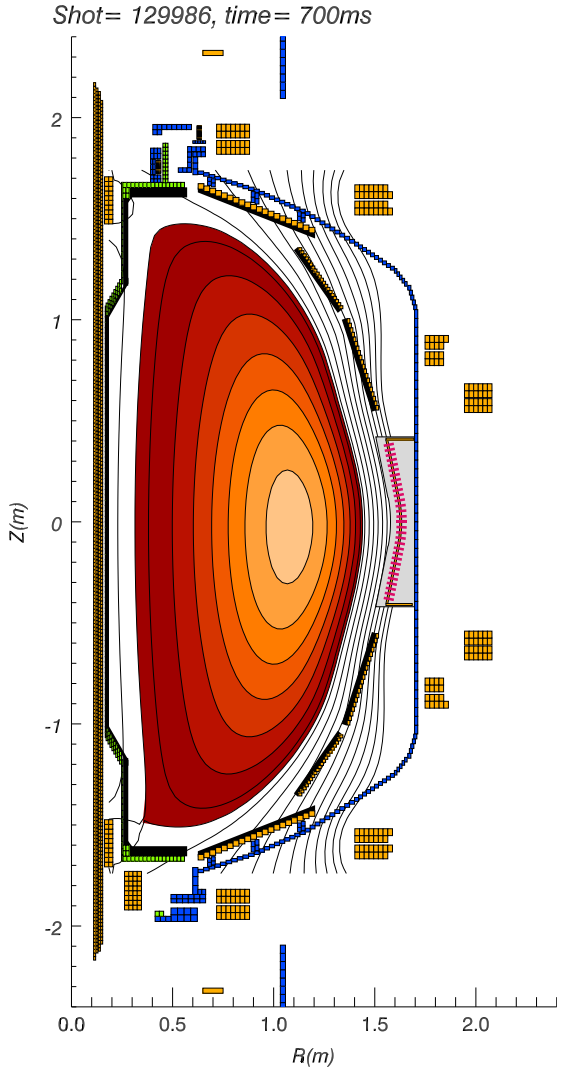

Figure 15. Reconstruction of a typical high $\kappa \sim 2.8$, high $\beta_p \sim 1.8$ equilibrium.

reduce the collisionality and thereby increase the beam driven current fraction to $f_{NBI} \sim 20\%$, roughly double that of the discharge shown in figure 15. The shot also achieved an NSTX record non-inductive current fraction of $f_{NI} \sim 71\%$. Whereas this shot used transient techniques to achieve this higher value of f_{NI}, it represents an important demonstration of the physics required to move towards the goal of $f_{NI} \sim 100\%$.

As mentioned in section 4, non-axisymmetric $n = 3$ EF control and $n = 1$ RFA suppression have been recently used as a standard operational tool to improve plasma discharge performance. This new capability was responsible for a dramatic increase in the reliability of long pulse operation, extending both the plasma duration and the peak pulse averaged β_N achievable in a plasma discharge. Shown in figure 16 are the average β_N (averaged over the plasma current flat-top) plotted versus the length of the flat-top, spanning the entire NSTX database for 2008. Black points represent discharges that did not have error field + RFA control, red points are plasmas that did have RFA control. The separation between the data points indicates the importance of controlling EFs at high plasma β. Whereas it is believed that lithium

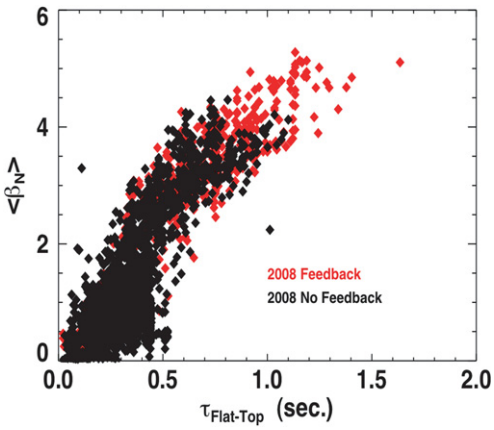

Figure 16. Comparison of β_N averaged over the plasma current flat-top plotted versus the plasma current flat-top for shots with (red) and without (black) $n = 3$ EF correction + $n = 1$ RFA suppression.

conditioning was also important in achieving this improved performance, statistical analysis similar to that performed in figure 16 did not show a similar separation in terms of β_N and pulse length between shots with lithium and those without lithium conditioning. This new non-axisymmetric field control capability has contributed to the longest plasma pulse ever created on a spherical tokamak device. The plasma discharge lasted for 1.8 s, with a plasma current flat-top of 1.6 s, limited only by heating constraints on the TF coil.

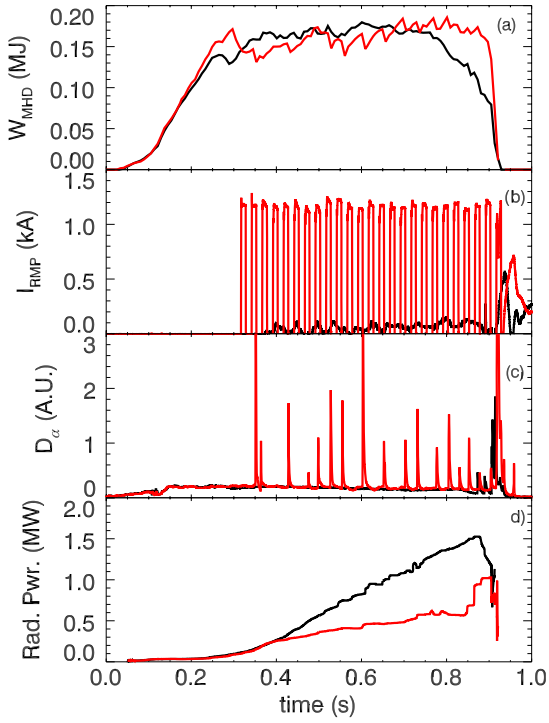

Figure 17. Comparison of an ELM-free discharge (black) with one to which $n = 3$ fields were added: (*a*) plasma stored energy for the entire discharge, (*b*) $n = 3$ current, (*c*) divertor D_α emission and (*d*) radiated power.

9. Research in direct support of ITER

9.1. The effect of 3D fields on ELM stability

Motivated by the need for additional information for ITER on the physics of 3D applied fields for ELM stabilization, experiments to modify edge stability and affect ELMs have been conducted in NSTX. The external non-axisymmetric coil set on NSTX mimics the ITER external coil set in both spectrum and normalized distance from the plasma, so NSTX has an optimal coil configuration with which to perform these important experiments to clarify this issue for ITER. Here the external coil set was used to apply $n = 2$, $n = 3$ and $n = 2 + 3$ fields to ELMy discharges. Whereas the signature of the ELMs on several diagnostics was indeed modified, mitigation of ELMs (i.e. reduction in ELM size) was not observed.

On the other hand, the application of $n = 3$ fields was observed to destabilize type I ELMs in ELM-free phases of discharges. This destabilization was observed to require a threshold perturbation strength, with stronger perturbations resulting in a higher ELM frequency. Substantial changes to the toroidal rotation profile were observed, qualitatively consistent with NTV non-resonant magnetic braking [14].

Short pulses of $n = 3$ fields were added to ELM-free H-mode discharges, produced by lithium wall coating, to controllably trigger ELMs and thereby reduce both the plasma density and the secular increase in the radiated power which usually occurs when ELMs are suppressed. Figure 17 compares the reference ELM-free discharge (black) with one to which short $n = 3$ perturbations were added (panel (*c*)). Note that the discharge with $n = 3$ field maintains high plasma stored energy for the entire discharge (panel (*a*)), has reduced line-average density (panel (*b*)), shows signatures of the ELMs on divertor D_α emission (panel (*c*)) and reduces the plasma radiated power (panel (*d*)). The triggered ELMs exhausted a substantial fraction of core stored energy ($\delta W / W_{tot} < 25\%$), but the average ELM size did decrease with elongation, suggesting a possible route for optimization. In addition, the $n = 3$ fields were 50–80% successful in triggering ELMs, depending on the discharge characteristics. The largest ELMs were typically observed after one of the pulses in the train failed to trigger an ELM. This suggests that further reduction in average ELM size would be obtained by improving the triggering efficiency. Finally the maximum triggering frequency is limited by the field penetration times; internal coils should greatly increase the maximum triggering frequency, leading to the prospect of smaller average ELM size.

9.2. Vertical stability studies for ITER

Experiments in NSTX have shown that a typical, highly robust double null plasma target has a measured maximum controllable vertical displacement $\Delta Z_{max} \sim 0.15$–0.24 m, corresponding to $\Delta Z_a \sim 23$–37% . Data from a scan of drift distances show that upward and downward-directed drifts have approximately the same maximum controllable displacement. The maximum displacement calculated for this equilibrium and control configuration using a TokSys [54] model developed in a collaboration between DIII-D and NSTX is found to be ~0.40 m, or $\Delta Z_a \sim 60\%$. The magnitude of this discrepancy is far greater than any observed sources of noise, and so is unlikely to be explained by such effects. A likely contributor to the discrepancy is inaccuracy in modelling the complex

non-axisymmetric passive structures of NSTX. Understanding the effect of complex non-axisymmetric conducting structures could be an important effect for determining vertical stability on ITER. Non-linear effects due to the large perturbation amplitudes on NSTX may also be important.

10. Summary

Substantial progress has been made towards achieving the primary mission of NSTX, which is to understand and utilize the advantages of the ST configuration by establishing attractive ST steady-state operating scenarios and configurations at high β. NSTX has also clarified some outstanding issues, such as the cause of electron transport, and the effect of plasma rotation on confinement and macroscopic stability, which are generic to toroidal fusion science, and has contributed to ITER both directly, via the ITER Design Review process, and through increased physics understanding. These advances have reinforced the case for an ST as a first-wall research device and as a potential fusion neutron producing facility, as well as for a potential reactor.

Turbulent density fluctuations have been observed in NSTX plasmas in the range of wave numbers $k_\perp \rho_e = 0.1$–0.4. The large values of $k_\perp \rho_i$, propagation in the electron drift direction, and a strong correlation with R/L_{T_e} exclude the ITG mode as the source of turbulence. Experimental observations and an agreement with numerical results from the linear gyro-kinetic GS2 code support the conjecture that the observed turbulence is driven by the ETG. Flow shear has been shown to effect the ion confinement in the edge of NSTX plasmas in a manner consistent with $E \times B$ reduction of ITG mode induced transport. Momentum transport has been measured and shown to be above that predicted by neoclassical theory, but consistent with the existence of residual ion-scale turbulence. Lithium evaporation has been used to coat the NSTX wall and has been an effective tool in increasing electron energy confinement, and suppressing ELMs, a key issue for ITER. The success of this coating technique has led NSTX to pursue a Liquid Lithium Divertor [55] as part of its near term research plan. The scaling of SOL fluxes has been measured on NSTX, an extremely important issue for future ST devices, such as the proposed NHTX [53]. Gas puffing experiments have successfully reduced the heat flux to the NSTX divertor plates, which can reach values of 10 MW m^{-2} similar to ITER. $n = 3$ EF correction has been combined with $n = 1$ RFA suppression, improving plasma performance measurably on NSTX. Flow shear has been shown to be an important effect in the appearance and growth of NTMs, clearly distinguished from the effect of rotation alone. The physics which determines the coupling of HHFW power through the SOL has been understood to be dominated by surface wave physics. This knowledge has been used to improve the efficacy and reliability on HHFW heating, and should be very helpful to successful RF heating experiments on ITER. The physics of EBW coupling has been understood and has been shown to be dominated by collisional damping at the mode conversion layer. It is important to note that lithium evaporation has been a crucial tool for making progress on the understanding of both of these important wave physics phenomena. Multi-mode fast particle MHD has been observed and identified as TAE avalanches on NSTX, which operates in the super Alfvénic regime. These avalanches have been modelled and the resultant loss of fast particles understood quantitatively. The ability to predict the physics of multi-mode Alfvén waves is crucial to ITER and all future burning plasmas experiments. NSTX has demonstrated the ability to couple traditional inductive current ramp to CHI current initiation and shown that plasma performance is similar to that without CHI. Even more important to the ST concept is the ability to maintain the plasma current in steady state. NSTX has demonstrated (1) the ability to operate with β_t and f_{bs} meeting the requirements of ST-CTF and NHTX using equilibria that match the requirements ($\kappa \sim 2.8$, $A \sim 1.6$–1.8). NSTX has also demonstrated a new record non-inductive current fraction with the increase coming from improved, neutral beam current drive efficiency. This improved efficiency is a result of operating at lower ν^*, motivating further research in this regime. Finally, NSTX has made important contributions to the ITER design review process in the areas of ELM stabilization using non-axisymmetric fields and in understanding vertical stability.

The substantial scientific productivity of NSTX is a testament to the importance of investigating physics in new regimes. By operating at low aspect ratio, new physics regimes are investigated and theories are tested and extended, which helps to clarify physics that is important not just to NSTX and low aspect ratio devices but to general toroidal fusion science.

Acknowledgments

This work was supported by the US Department of Energy Grant under contract number DE-AC02-76CH03073.

References

References presented below as papers at this conference are available online at http://www-naweb.iaea.org/napc/physics/FEC/FEC2008/html/index.htm

[1] Peng Y.-K.M and Strickler D.J 1986 *Nucl. Fusion* **26** 769
[2] Najmabadi F. and the ARIES Team 2003 *Fusion Eng. Des.* **65** 143
[3] Peng Y.-K.M. *et al* 2005 *Plasma Phys. Control. Fusion* **47** B263
[4] Ono M. *et al* 2000 *Nucl. Fusion* **40** 557
[5] Coppi B. and Rewoldt G. 1976 *Advances in Plasma Physics* vol 6 ed A. Simon and W.B. Thompson (New York: Wiley) p 421
[6] Horton W. 1999 *Rev. Mod. Phys.* **71** 735
[7] Connor J.W. and Wilson H.R. 1994 *Plasma Phys. Control. Fusion* **36** 719
[8] Mazzucato E. 2003 *Phys. Plasmas* **10** 753
[9] Mazzucato E. *et al* 2008 *Phys. Rev. Lett.* **101** 075001
[10] Mazzucato E. *et al* Turbulent fluctuations with the electron gyro-scale in NSTX plasmas Paper EX/10-2Ra
[11] Kotschenreuther M., Rewoldt G. and Tang W.M. 1995 *Comput. Phys. Commun.* **88** 128
[12] Jenko F., Dorland W. and Hammett G.W. 2001 *Phys. Plasmas* **8** 4096
[13] Kaye S.M. *et al* 2007 *Nucl. Fusion* **47** 499
[14] Zhu W. *et al* 2006 *Phys. Rev. Lett.* **96** 225002
[15] Hawryluk R.J. 1980 *Physics of Plasmas Close to Thermonuclear Conditions* vol 1 (Brussels: CEC) p 19
[16] Wang W., Tang W.M., Hinton F.L., Zakharov L.E., White R.B. and Manickam J. 2004 *Comput. Phys. Commun.* **164** 178
[17] Solomon W.M. *et al* 2008 *Phys. Rev. Lett.* **101** 065004

[18] Kaye S. *et al* Momentum transport in electron-dominated spherical torus plasmas Paper EX/3-2
[19] Kugel H.W. *et al* 2008 *Phys. Plasmas* **15** 056118
[20] Mansfield D. *et al* 2009 Transition to ELM-free improved H-mode by lithium deposition on NSTX graphite divertor surfaces *J. Nucl. Mater.* at press
[21] Maingi R. *et al* 2003 *Nucl. Fusion* **43** 969
[22] Soukhanovskii V.A. *et al* 2007 *J. Nucl. Mater.* **363–365** 432
[23] Gates D.A. *et al* 2006 *Phys. Plasmas* **13** 056122
[24] Soukhanovskii V.A. *et al* 2009 *Phys. Plasmas* **16** 022501
[25] Ahn J.W. *et al* 2008 *Phys. Plasma* **15** 122507
[26] Maingi R. *et al* 2007 *J. Nucl. Mater.* **363–365** 196
[27] Ahn J.W., Maingi R., Boedo J., Soukhanovskii V. and the NSTX team *et al* 2009 Dependence of SOL widths on plasma current and density in NSTX H-mode plasmas *J. Nucl. Mater.* at press
[28] Soukhanovskii V. *et al* Divertor heat flux mitigation in high-performance H-mode plasmas in the National spherical torus experiment Paper EX/P4-22
[29] Menard J.E. *et al* 2007 *Nucl. Fusion* **47** S645
[30] Menard J.E. *et al* 2005 *Nucl. Fusion* **45** 539
[31] Sontag A.C. *et al* 2007 *Nucl. Fusion* **47** 1005
[32] Sabbagh S.A. *et al* 2006 *Phys. Rev. Lett.* **97** 045004
[33] Hu B., Betti R. and Manickam J. 2005 *Phys. Plasmas* **12** 057301
[34] Sabbagh S.A. *et al* Advances in global MHD mode stabilization research on NSTX Paper EX/5-1
[35] Shaing K.C., Hirschman S.P. and Callen J.D. 1986 *Phys. Fluids* **29** 521
[36] Buttery R. *et al* 2008 *Phys. Plasmas* **15** 056115
[37] Gerhardt S. *et al* 2008 *Nucl. Fusion* **48** 032001
[38] Ryan P.M. *et al* 2008 *Proc. 35th EPS Conf. on Plasma Physics (Hersonissos, Greece, 9–13 June 2008)* vol 32D (ECA) P-1.108 http://epsppd.epfl.ch/Hersonissos/pdf/P1_108.pdf
[39] Hosea J. *et al* 2008 *Phys. Plasmas* **15** 056104
[40] Phillips C.K. *et al* Spectral effects on fast wave core heating and current drive Paper EX/P6-25
[41] LeBlanc B.P. *et al* 2005 *16th Topical Conf. on RF Power in Plasmas (Park City, UT, USA, 2005)* ed S.J. Wukitch and P.T. Bonoli *AIP Conf. Proc.* **787** 86
[42] Diem S.J. *et al* 2006 *Rev. Sci. Instrum.* **77** 10E919
[43] Diem S.J. *et al* Investigation of electron Bernstein wave (EBW) coupling and its critical dependence on EBW collisional loss in high-β, H-mode ST plasmas Paper EX/P6-17
[44] Preinhaelter J. *et al* 2006 *Rev. Sci. Instrum.* **77** 10F524
[45] Berk H.L., Breizman B.N. and Pekker M. 1995 *Phys. Plasmas* **2** 3007
[46] Fredrickson E.D. *et al* 2006 *Nucl. Fusion* **46** S296
[47] Fredrickson E.D. *et al* Toroidal Alfvén eigenmode avalanches in NSTX Paper EX/6-3
[48] White R.B. and Chance M.S. 1984 *Phys. Fluids* **27** 2455
[49] White R.B. 1990 *Phys. Fluids* B **2** 845
[50] Jarboe T.R. 1989 *Fusion Technol.* **15** 7
[51] Raman R. *et al* 2005 *Nucl. Fusion* **45** L15–L19
[52] Raman R. *et al* Solenoid-free plasma start-up in NSTX using transient CHI Paper EX/P6-10
[53] Goldston R.J. *et al* An experiment to tame the plasma material interface Paper FT/P3-12
[54] Humphreys D.A. *et al* 2007 *Nucl. Fusion* **47** 943
[55] Kaita R. *et al* Plasma performance improvement with lithium-coated plasma-facing components in NSTX Paper EX/P4-9